Hydrodynamics and mixing in continuous oscillatory flow reactors-Part II: Characterisation methods

Alex Mazubert, David Fletcher, Martine Poux, Joelle Aubin

Hydrodynamics and mixing in continuous oscillatory flow reactors—Part II: Characterisation methods

A. Mazubert[a,b], D.F. Fletcher[c], M. Poux[a,b], J. Aubin[a,b,*]

[a] University of Toulouse, INPT/UPS, Laboratoire de Génie Chimique, 4 Allée Emile Monso, BP-31243, 31432 Toulouse, France
[b] CNRS, Laboratoire de Génie Chimique, 31432 Toulouse, France
[c] School of Chemical and Biomolecular Engineering, The University of Sydney, NSW 2006, Australia

A B S T R A C T

This work presents and exploits quantitative measures to better quantify the performance of oscillatory baffled reactors, being complementary to simple vector plots and shear strain rate fields. Novel performance criteria, including radial and axial fluid stretching and mixing, as well as the shear strain rate history of fluid elements have been developed and used to compare the performance of five different baffle designs, namely single orifice baffles, disc-and-donut baffles and three novel variations of helical blades. Analysis of residence time distributions has also been used to evaluate the geometries. The performance measures highlight that the disc-and-donut baffles can provide significant shear strain rates, which could be useful for multiphase applications, but also significant axial dispersion that is comparable with that for the single orifice baffles. The results also suggest that helical blade designs could be promising for decreasing axial dispersion, whilst maintaining significant levels of shear strain rate.

Keywords:
Mixing
Process intensification
Oscillatory baffled reactors
Oscillatory flow

1. Introduction

In Part I of this series [1], time-resolved laminar CFD simulations have been performed to study the flow generated in five oscillatory baffled reactor (OBR) designs, three of which are novel compared with the single orifice baffles or disc-and-donut baffles that have been traditionally used for this type of device. The flow generated by these designs has been assessed by examining instantaneous velocity fields, shear strain rate fields and pressure drop.

This study highlighted the complex flow behavior and the formation of vortices in the reactor due to both flow blockage by the baffle design and flow reversal. Indeed, depending on the baffle geometry, there is more or less fluid recirculation, dominant axial flow and shear strain rate variation. The disc-and-donut baffles generate multiple vortices and the helical blade designs create a complex 3D flow with a significant transverse component. In terms of shear strain rates, which are of interest for multiphase applications, the disc-and-donut baffles and the helical blade baffles provide the highest values, which are more than two times greater than those generated by the single orifice design. It is interesting to note however that the maximum strain rates are localised and occupy relatively small volumes in the reactor; only the disc-and-donut baffles provide substantial spatial variation of shear strain rate. This means that only a small amount of fluid passing through the reactor may experience high shear stress. The work also showed that the baffle design has a huge impact on pressure drop, which is as expected. The disc-and-donut design causes the highest pressure drop, which is greater by about a factor of five than that with the single orifice baffles. The pressure drop generated by helical baffles is approximately half that of the disc-and-donut design. Indeed, although the ensemble of the results provide knowledge on the flow mechanisms and operating characteristics of OBRs, it is clearly difficult to conclude on the impact of baffle design on the performance of the reactor with velocity and shear strain rates alone.

As previously reported in the introduction of Part I, the majority of the studies in the literature describe the flow generated in OBRs in a qualitative manner using planar velocity fields and velocity profiles [2–5] or shear strain rate fields [6]. A significant number of studies have also evaluated the performance of OBRs in terms of axial dispersion via the analysis of residence time distributions [7–13]. The general observation of these studies is that for oscillatory Reynolds numbers (Re_O) greater than approximately 200, the axial dispersion coefficient increases linearly when with increasing Re_O, being proportional

* Corresponding author at: CNRS, Laboratoire de Génie Chimique, 31432 Toulouse, France.
E-mail address: joelle.aubincano@ensiacet.fr (J. Aubin).

Nomenclature

A	Amplitude of oscillation (m)
d	Tube diameter (m)
D_{ax}	Axial dispersion coefficient ($m^2\,s^{-1}$)
E	Residence time distribution (s^{-1})
f	Frequency of oscillation (Hz)
$\boldsymbol{F}_D$	Drag force (N)
I	Stretching distance (m)
L	Length of tube (m)
m_p	Mass of particle (kg)
n_{pairs}	Number of particle pairs
N_w	Weighted number of particles
Pe	Péclet number ($u\,L/D_{ax}$)
Q	Volumetric flow rate ($m^3\,s^{-1}$)
R	Radial location (m)
Re_{net}	Net Reynolds number ($u_{net}d\rho/\mu$)
Re_O	Oscillatory Reynolds number ($2\pi fAd\rho/\mu$)
S_{ij}	Shear strain rate tensor (s^{-1})
SSR	Magnitude of shear strain rate (s^{-1})
STD	Standard deviation
t	Time (s)
t_m	Mean residence time (s)
u	Characteristic speed of flow ($m\,s^{-1}$)
$\boldsymbol{v}$	Velocity vector ($m\,s^{-1}$)
V	Reactor volume (m^3)
X, Y, Z	Cartesian coordinates (m)
$\boldsymbol{y}$	Particle location (m)

Greek symbols

μ	Dynamic viscosity (Pa s)
ρ	Fluid density ($kg\,m^{-3}$)
σ_l	Standard deviation of stretching distance (m)
τ	Space time (V/Q) (s)

Subscripts

0	Constant component
net	Net
o	Oscillatory

to the product $A.f$. For $Re_O < 200$, however, a decrease in Re_O also causes an increase in the axial dispersion coefficient such that there is a minimum axial dispersion as a function of Re_O. Smith and Mackley [9] explain the minimum in the axial dispersion coefficient due to the interaction of net flow and oscillatory flow whereby significant radial mixing is generated without excessive axial mixing. They have also shown that an increase of the net Reynolds number (Re_{net}) also causes an increase in the axial dispersion coefficient.

The main objective of this paper is to develop alternative methods that allow OBRs to be characterised and assessed in terms of different performance criteria: radial and axial fluid stretching and mixing, and shear strain rate history. The performance of these methods is then demonstrated using the five different reactor geometries presented in Part 1. A Lagrangian particle tracking method has also been used to carry out an analysis of the residence time distribution, which completes various studies in the literature [9–12,14,15].

2. Flow computation and particle tracking

The methodology used to perform the flow simulations was described fully in Part 1 of this paper [1]. In addition to the usual analysis of the flow field variables we also performed Lagrangian particle tracking to provide additional information. We used particles having the same density as the fluid and a diameter of 1 micron which have a Stokes numbers of $O(10^{-5})$ and therefore follow the fluid faithfully. With this method there is no interaction between particles and no physical and little numerical diffusion. The Lagrangian approach introduces no artificial diffusion and in Part I we showed the flow results are mesh and time-step independent so we can reasonably expect the numerical diffusion in the velocity field to be very low. The particle behavior is determined by integration of the kinematic and momentum balance equations for each particle, which take the form

$$\frac{d\mathbf{y}}{dt} = \mathbf{v}, m_p\frac{d\mathbf{v}}{dt} = \mathbf{F}_D \tag{1}$$

where $\mathbf{y}$ is the particle location, $\mathbf{v}$ its velocity, t is time, m_p is the mass of the particle $\boldsymbol{F}_D$ is the drag force, which was modeled using the Schiller Naumann model. These equations were integrated using a fourth-order Runge–Kutta scheme with adaptive step size.

A line of such particles was released along the tube radius at a particular axial location (X_0), with their initial velocity set to that of the local fluid velocity. The number of initial particle locations along the line was set at 2484 for 2D geometries and 4968 for 3D geometries and this number of particles proved sufficient to characterise the flow. In addition to recording the particle travel time, location and velocity components, a particle scalar was used to store the local strain rate of the fluid. At the end of the run data

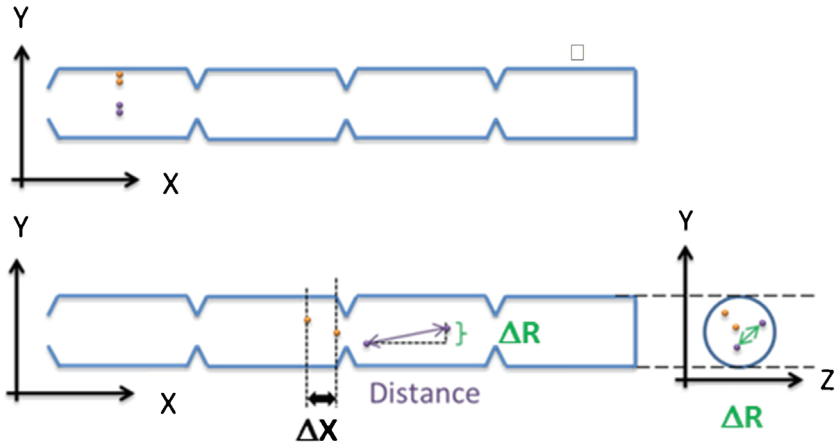

Fig. 1. Principle of the radial and axial stretching calculations. At a given time, the axial distance ΔX, and the radial distance ΔR separating each pair of particles are calculated.

for each track were exported and gave a complete history of the conditions experienced by the particle, which represents that of the fluid originating at the initial location of the particle.

3. Characterisation techniques

3.1. Radial and axial fluid stretching

This technique follows the radial and axial distances separating two initially adjacent particles as a function of time. It is used to quantify radial and axial mixing separately. Fluid elements that experience significant stretch in the radial direction are in zones of good radial mixing, whereas fluid elements with very little stretching experience poor radial mixing. Small stretching distances in the axial direction, however, highlight near plug-flow behavior. On the other hand high amounts of stretching in the axial flow direction suggest a wide residence time distribution.

Calculations are performed for pairs of initially adjacent particles. The time evolution of the distance separating the pair of particles is determined at every time step for 50 s. The principle of the calculations for one pair of particles is described by the following equations and the schematic diagram given in Fig. 1.

At time t, $\Delta X = |X_{\text{particleA}} - X_{\text{particleB}}|$, where X is the axial coordinate of the particle.

$\Delta X(t)$ is then integrated for each pair of particles, giving an average value of stretching $I_{\Delta X}$:

$$I_{\Delta X} = \frac{1}{t_n}\sum_{i=0}^{t_n}\frac{\Delta X_{i+1} + \Delta X_i}{2}(t_{i+1} - t_i) \tag{2}$$

$\bar{I}_{\Delta X}$ is the average value of $I_{\Delta X}$ for all particle pairs and is calculated as:

$$\bar{I}_{\Delta X} = \frac{1}{n_{\text{pairs}}}\sum_{j=1}^{n_{\text{pairs}}} I_{\Delta X_j} \tag{3}$$

and the standard deviation σ_I is:

$$\sigma_I = \sqrt{\frac{1}{n_{\text{pairs}}}\sum_{j=1}^{n_{\text{pairs}}}\left(I_{\Delta X_j}\right)^2 - \left(\bar{I}_{\Delta X}\right)^2} \tag{4}$$

An analogous calculation is made for stretching in the radial direction R, where $R = \sqrt{\left(Y^2 + Z^2\right)}$.

3.2. Residence time distribution

The RTD for the fluid flowing through the various OBR geometries was calculated by determining the particle trajectories and by recording the particle residence times over a defined length of the OBR geometry. The residence time distribution, $E(t)$, as described by Fogler [16], is then calculated as:

$$E(t) = \frac{\Delta N_w}{N_w}\frac{1}{\Delta t} \tag{5}$$

where ΔN_w is the number of particles that have a residence time in the reactor between time t and $t + \Delta t$ each weighted by their initial velocity normalized by the maximum velocity in the tube, and N_w is the total weight number of particles released in the reactor. This approach has already been successfully employed for RTD analysis in continuous microreactors by Aubin et al. [17]. From $E(t)$, the first and second moments, i.e. the mean residence time t_m and the variance σ^2_{RTD} can be determined. For open systems the mean residence time and the variance are related to the reactor Péclet number Pe, following:

$$\frac{\sigma^2_{\text{RTD}}}{t_m^2} = \frac{2}{\text{Pe}} + \frac{8}{\text{Pe}^2} \tag{6}$$

The Péclet number is defined as:

$$\text{Pe} = \frac{uL}{D_{ax}} \tag{7}$$

where L is the length of the tube and D_{ax} is the axial dispersion coefficient. The principle of the determination of Péclet number and axial dispersion coefficient is illustrated in Fig. 2. The characteristic length L corresponds to the distance between the plane where the particles are released ($X = X_0$) and the plane where the residence times of particles are recorded ($X = X_{\text{detection}}$).

3.3. Shear strain rate history

Evaluation of the shear strain rates (SSR) generated in the OBR are important for liquid-liquid dispersion and emulsion applications where sufficiently high shear rates are required for droplet break-up, or for operations involving biological cultures where shear strain rates need to be controlled to avoid cell damage. The

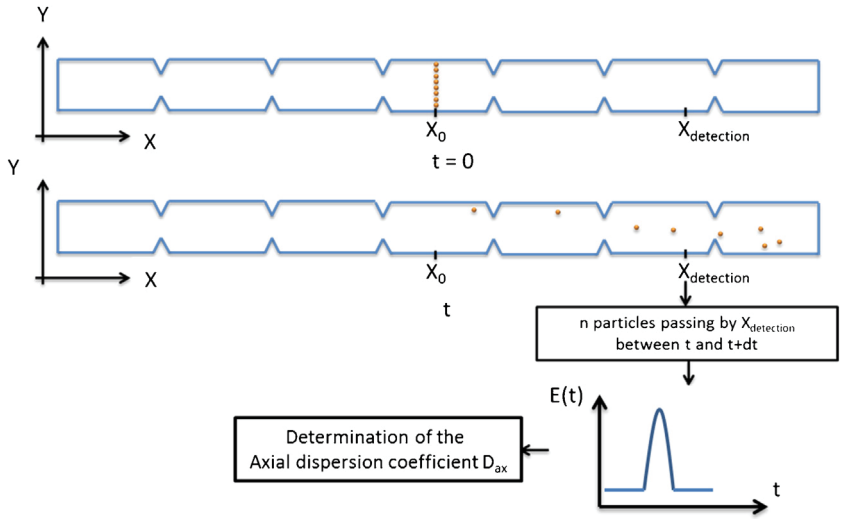

Fig. 2. Particles that are evenly distributed across the radius of the tube are released at X_0. The number of particles passing $X_{\text{detection}}$ between at different times are recorded to determine the residence time distribution function $E(t)$ from which the axial dispersion coefficient D_{ax} is calculated.

shear strain rate tensor for an incompressible fluid is given by:

$$S_{ij} = \frac{1}{2}\left(\frac{\partial u_i}{\partial x_j} + \frac{\partial u_j}{\partial x_i}\right) \quad (8)$$

which gives the following equation for the magnitude of the shear strain rate:

$$\mathrm{SSR} = \left[2\frac{\partial u_i}{\partial x_j}S_{ij}\right]^{1/2} \quad (9)$$

Although local values of shear strain rate can be directly obtained from the CFD simulations, they do not provide statistical information on the duration and volume of the flow that experiences different ranges of shear rates. This can be done however by following the shear strain rate experienced by each tracer particle on its trajectory through the reactor. At every time step, the strain rate magnitude is recorded for each particle. The maximum strain rate and the average strain rate for each particle over time are then calculated. Finally, the global mean strain rate experienced by the ensemble of particles is determined.

4. Verification of characterisation methods

In addition to verifying that the solution is mesh independent, which was shown in Part I of this study [1]. the independency of the performance characteristics (determined by particle tracking techniques) on mesh size and the number of tracking particles used was also checked. The effect of these parameters, as well as the reactor length and the injection position of the tracer particles, on fluid stretching, the axial dispersion coefficient and the strain rate history were investigated.

4.1. Influence of the mesh size

The influence of the mesh size on radial and axial fluid stretching and on residence time distribution calculated in the OBR with single orifice plates and with a single helical baffle with $A = 16.5$ mm and $f = 1.05$ Hz is presented in Table 1. The results show that the mean values of radial and axial stretching, as well as their standard deviation, and the axial dispersion coefficient and mean residence time hardly vary when computed on the different meshes. The relative difference of the values obtained on the different meshes are below 6% for the 2-dimensional mesh used for the orifice plate geometry and less than 1% for the 3-dimensional mesh used for the single helical baffle reactor. Moreover, the mesh size has also shown to have no influence on the average and maximum particle strain rates, and the standard deviation; the relative differences of these values calculated on different mesh sizes is less the 0.4%. From these results, it can be concluded that the calculated values are independent of the mesh sizes studied here. As a result, the coarser grids have been used for the study.

4.2. Influence of number of particles

Table 2 shows the influence of the number of particles released at X_0 on the statistics concerning the fluid stretching, the axial dispersion coefficient and mean residence time, and strain rate history in the OBR with single orifice plates with oscillating conditions $A = 16.5$ mm, $f = 1.05$ Hz. The particles are released at $X_0 = 0.248$ mm and detected at $X_{\mathrm{detection}} = 404$ mm. It can be seen that there are non-negligible differences in the radial and axial stretching values when using only 150 particles compared with 2484 particles; the relative difference between the values calculated for different particle numbers is around 10%. When comparing the values calculated using 2484 and 4968 particles, the relative difference for all quantities is in general less than 2% and therefore 2484 particles where used for the comparative study.

4.3. Influence of reactor length and position of particle injection

Due to the oscillatory (or pulsed) motion of the flow in the reactor, the axial position where the tracking particles are released, X_0, and where they are detected, $X_{\mathrm{detection}}$, for residence time calculations have to be carefully chosen. Indeed if the X_0 and $X_{\mathrm{detection}}$ are too close to the tube inlet and outlet, respectively, the particles can leave the computational domain due to the oscillating flow, but cannot re-enter. To avoid this, the tube has to be sufficiently long and X_0 and $X_{\mathrm{detection}}$ must be at a sufficient distance from the inlet and outlet, respectively. Furthermore, the simulation time must to be long enough to allow a maximum number of particles to flow from X_0 to $X_{\mathrm{detection}}$. It was found that 98% of the particles released at X_0 reached $X_{\mathrm{detection}}$ within 50 s and therefore the simulation time was set to 50 s.

To determine the reactor length and the positions of X_0 and $X_{\mathrm{detection}}$, that minimize the number of particles that leave the computational domain, tests have been carried out for the single orifice baffle geometry with $A = 16.5$ mm, $f = 1.05$ Hz and a net velocity of 1.405×10^{-2} m s^{-1}. Two different tube lengths ($L = 310$ mm and $L = 570$ mm) comprising 10 and 20 baffles each, have been compared. The position X_0 and $X_{\mathrm{detection}}$ has been varied from 64 mm to 272 mm, i.e. approximately 20–50% of the reactor length, from the inlet. $X_{\mathrm{detection}}$ has been varied between 85 mm and 248 mm from the outlet, corresponding to positions that are 40–83% of the reactor length.

Fig. 3 shows the fraction of total tracking particles detected at $X_{\mathrm{detection}}$ after a simulation time of 50 s for varied values of X_0, $X_{\mathrm{detection}}$ and reactor length. For the case where $X_0/L = 0.21$, the reactor length is 310 mm and it can be seen that fraction of particles measured at $X_{\mathrm{detection}}$ is not greater than 95%. Indeed, it was observed that some particles leave the computational domain via the inlet and outlet, but do not re-enter the domain, which is physically incorrect. When the reactor length is increased to 570 mm, which corresponds to the points where $X_0/L = 0.30$, 0.44 and 0.48, the fraction of particles detected at $X_{\mathrm{detection}}$ is greater than 98% for five of the eight cases tested. It can also be seen that the further X_0 and $X_{\mathrm{detection}}$ are from the tube inlet and outlet, respectively, the lower the particle loss. As a result, a criterion for the choice of tube length is set such that the fraction of particles detected at $X_{\mathrm{detection}}$ is greater than 98% and X_0 and $X_{\mathrm{detection}}$ are positioned such that the distance between the two is maximized. Based on this, the reactor length was set to 570 mm and the

Table 1
Influence of the mesh size on radial and axial fluid stretching and on parameters related to residence time distribution.

Baffle design	Mesh size (# cells)	$\bar{l}_{\Delta X}$ (mm)	$\sigma_{l_{\Delta x}}$ (mm)	$\bar{l}_{\Delta R}$ (mm)	$\sigma_{l_{\Delta R}}$ (mm)	D_{ax} (m^2 s^{-1})	t_{m} (s)
Single orifice plate	36,000	67.6	36.5	1.87	0.55	2.05×10^{-3}	5.8
	63,000	65.3	37.7	1.80	0.55	2.17×10^{-3}	5.4
Single helical baffle	902,000	49.2	26.3	1.92	0.41	1.29×10^{-3}	6.1
	1,579,000	49.5	26.4	1.93	0.43	1.28×10^{-3}	6.2

Table 2
Influence of the number of particles on average fluid stretching via ΔX and ΔR and standard deviation, the axial dispersion coefficient D_{ax}, the mean residence time t_m, and the time-averaged and maximum fluid strain rate with their associated standard deviations.

	Number of tracking particles			Relative difference (%)	
	150	2484	4968	150 vs 2484	2484 vs 4968
$\bar{I}_{\Delta X}$ (mm)	75.1	67.6	66.3	10.0	1.9
$\sigma_{I_{\Delta X}}$ (mm)	33.0	36.5	37.0	10.6	1.4
$\bar{I}_{\Delta R}$ (mm)	2.1	1.9	1.9	9.5	0.0
$\sigma_{I_{\Delta R}}$ (mm)	0.64	0.55	0.54	14.1	1.8
D_{ax} ($m^2 s^{-1}$)	2.03×10^{-3}	2.05×10^{-3}	2.11×10^{-3}	1.0	2.9
t_m (s)	6.2	5.8	5.7	7.3	0.9
Mean SSR (s^{-1})	44.2	44.2	43.4	0.0	1.8
STD mean SSR (s^{-1})	5.4	6.3	6.1	16.7	3.2
Max SSR (s^{-1})	299.3	296.2	296.2	1.0	0.0
STD max SSR (s^{-1})	39.6	42.7	44.7	7.8	4.7

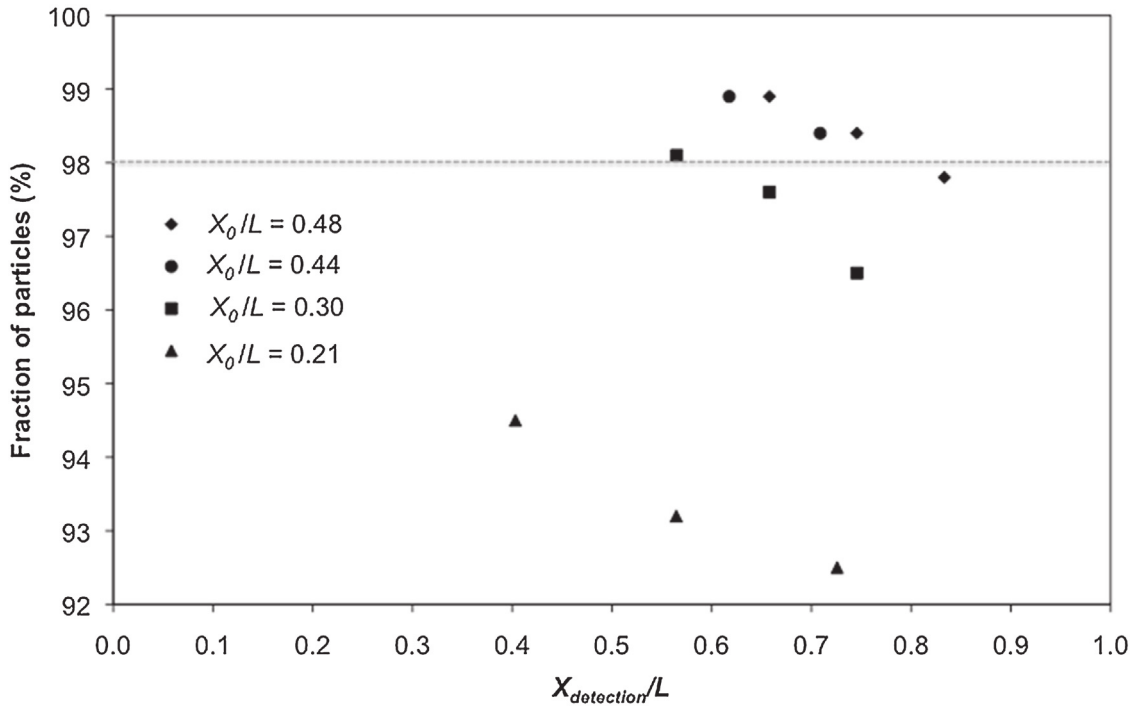

Fig. 3. Influence of the positions where tracking particles are released (X_0) and detected ($X_{detection}$) on the number of particles that pass $X_{detection}$ for the analysis. Note that $X_0/L = 0.21$ corresponds to a reactor length L equal to 310 mm, whereas the other X_0/L values are for $L = 570$ mm.

positions $X_0 = 248$ mm and $X_{detection} = 404$ mm for all of the following simulations. The fraction of particles detected at $X_{detection}$ also has a major role in the accuracy of the calculated axial dispersion coefficient as it can be seen in Fig. 4. Indeed the value of the axial dispersion coefficient increases by a factor of two when the fraction of particles increases from 92–95% to 98%. The uncertainty of the axial dispersion coefficient has been estimated at 8%.

5. Performance characterisation of baffle geometries

5.1. Radial and axial fluid stretching

Fig. 5 shows the average stretching normalised by the tube diameter, $I_{\Delta X}^*$ and $I_{\Delta R}^*$, of each fluid element over 50 s as a function of the initial normalised radial position in the OBR with single orifice baffles. For good mixing, the OBR geometry should promote stretching in the radial direction but minimize axial stretching, such that plug-flow behavior is achieved. It can be seen from Fig. 5 that in general the axial stretching is more than 100 times greater than the radial stretching for the single orifice baffle geometry.

The average axial and radial stretching distances (normalised by the tube diameter)—$\bar{I}_{\Delta X}^*$ and $\bar{I}_{\Delta R}^*$—for the different baffle geometries as a function of oscillatory Reynolds number are shown in Fig. 6. It can be seen that $\bar{I}_{\Delta X}^*$ increases linearly with the oscillatory Reynolds number and that mean axial stretching distance after 50 s is equivalent to several tube diameters. Moreover, the standard deviation, represented by the error bars in Fig. 6, is significant (being more than half of the average value), which means that the stretching distances are rather inhomogeneous, as shown in Fig. 5 for the single orifice baffle geometry. Clearly, there is little difference in the axial stretching distances provided by the single orifice baffles and the disc-and-donut

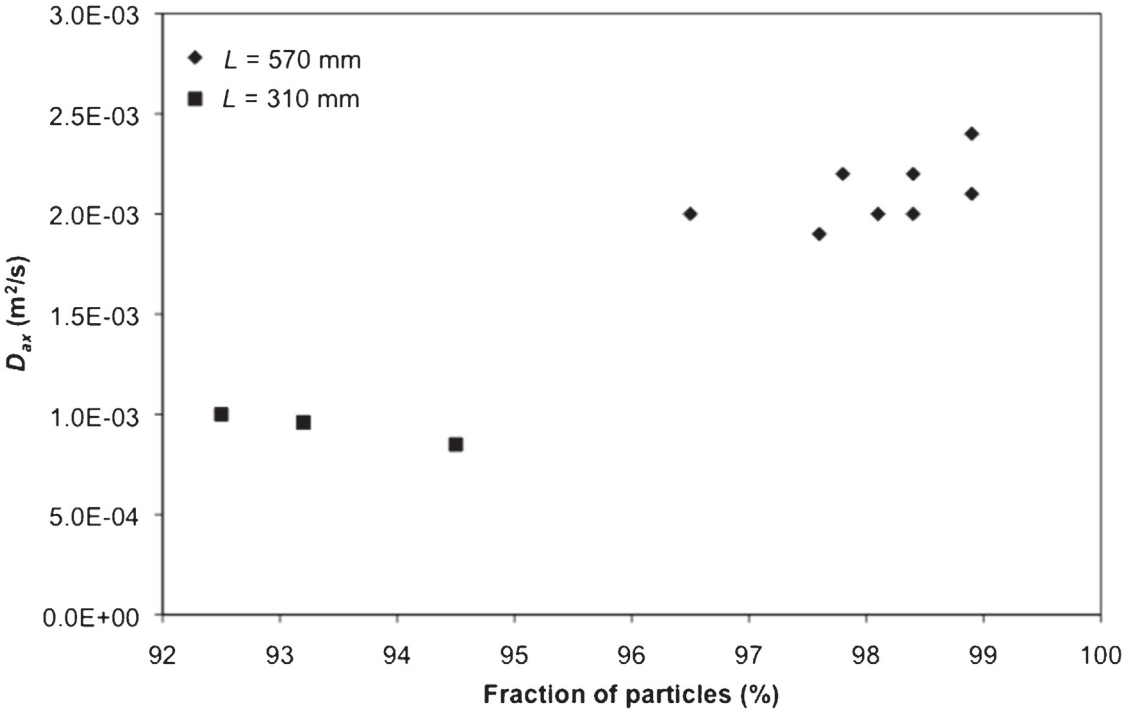

Fig. 4. Influence of the fraction of tracking particles recorded on the axial dispersion coefficient.

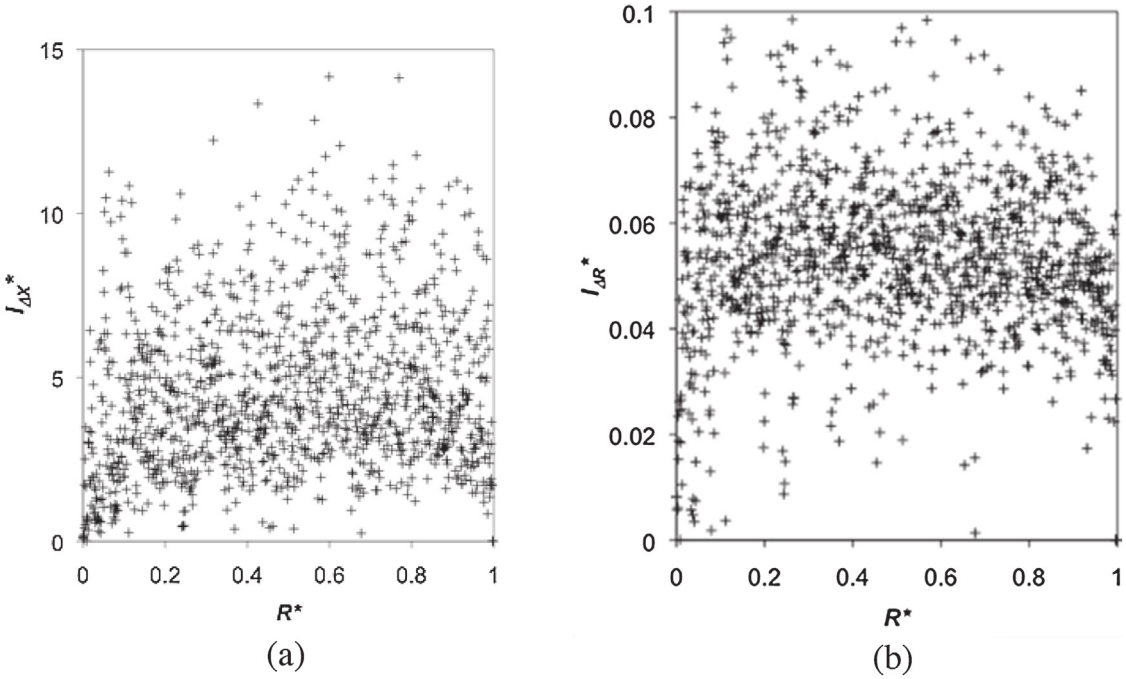

Fig. 5. Axial (a) and radial (b) stretching of fluid elements normalized by the tube diameter as a function of their initial normalised radial position for the single orifice baffle geometry with an oscillation amplitude of 16.5 mm and a frequency of 1.05 Hz.

baffles. On the other hand, it is observed for simulations performed with the helical blade geometries at $Re_O = 42$ that the mean axial stretching distance decreases by approximately 20–30% and the standard deviation is also lower. The lowest values are obtained for the alternating helical baffle. Although it is not possible to generalise the improved flow performance with the helical geometries, these results demonstrate the capacity of the method to detect a difference in flow performance provided by the different equipment.

The trend for radial stretching distances is slightly different; $\bar{I}_{\Delta R}^*$ initially increases with increasing oscillatory Reynolds number and then remains constant from approximately $Re_O = 40$. The radial

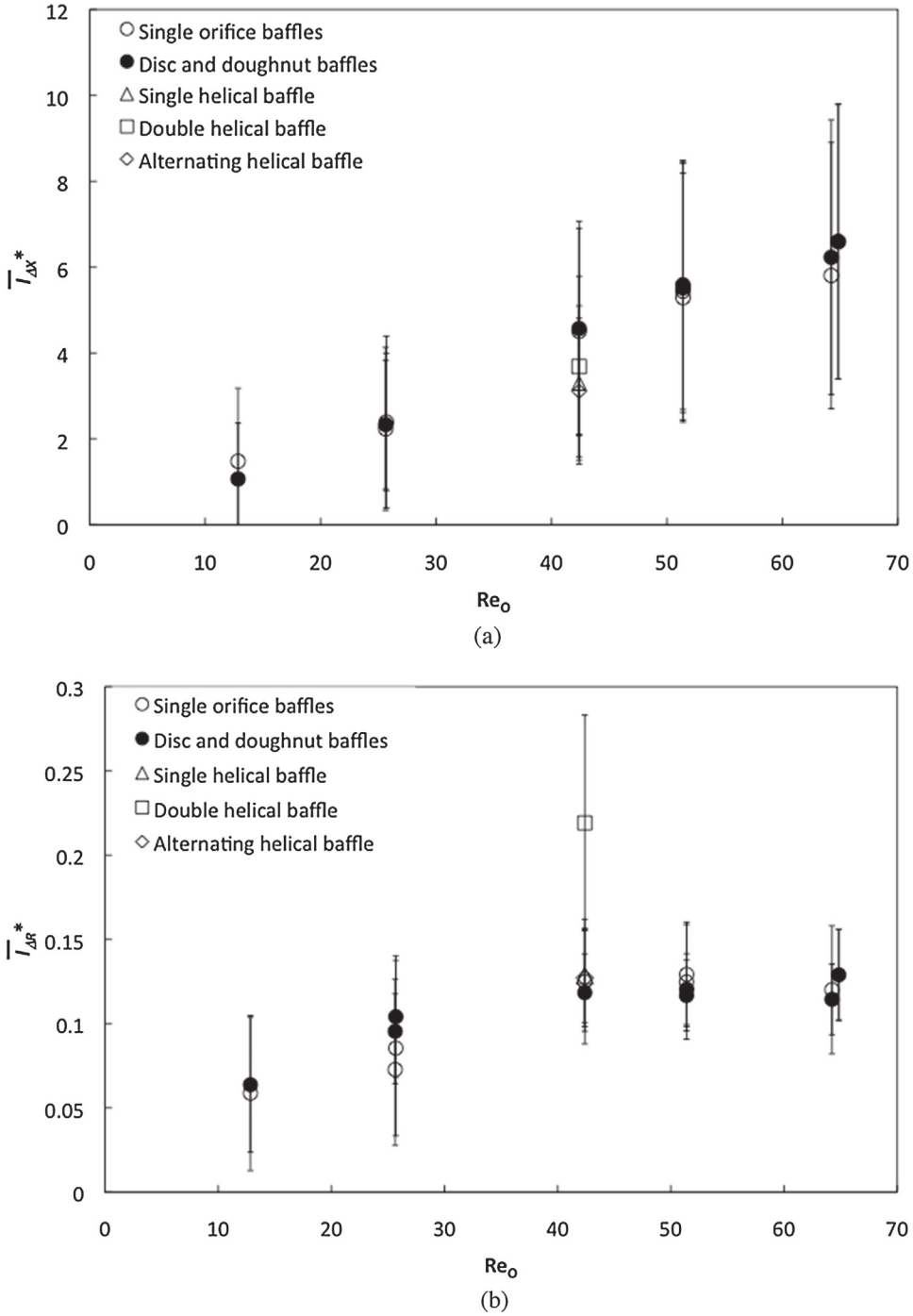

Fig. 6. Mean (a) axial and (b) radial stretching (normalised by tube diameter) as a function of the oscillatory Reynolds number and for different baffle geometries. The error bars represent the normalised standard deviation.

stretching distances are also much smaller than the axial distances, typically ranging between 5% and 15% of the tube diameter and the standard deviations are also smaller. Apart from the alternating helical blade, the baffle geometry has little effect on the radial stretching distances. For the oscillatory Reynolds number tested, the alternating helical blade however enables the mean axial stretching distance to be increased by a factor of two, compared with the other geometries.

5.2. Residence time distribution and axial dispersion coefficient

The residence time distribution $E(t)$ of an ideal plug-flow reactor is an infinitely high peak with zero width. The dispersion model, which involves an axial dispersion coefficient D_{ax}, allows the non-ideal behavior of the reactor to be represented. D_{ax} can be calculated from the residence time distribution, which has a finite width and height. The residence time distributions $E(t)$ obtained

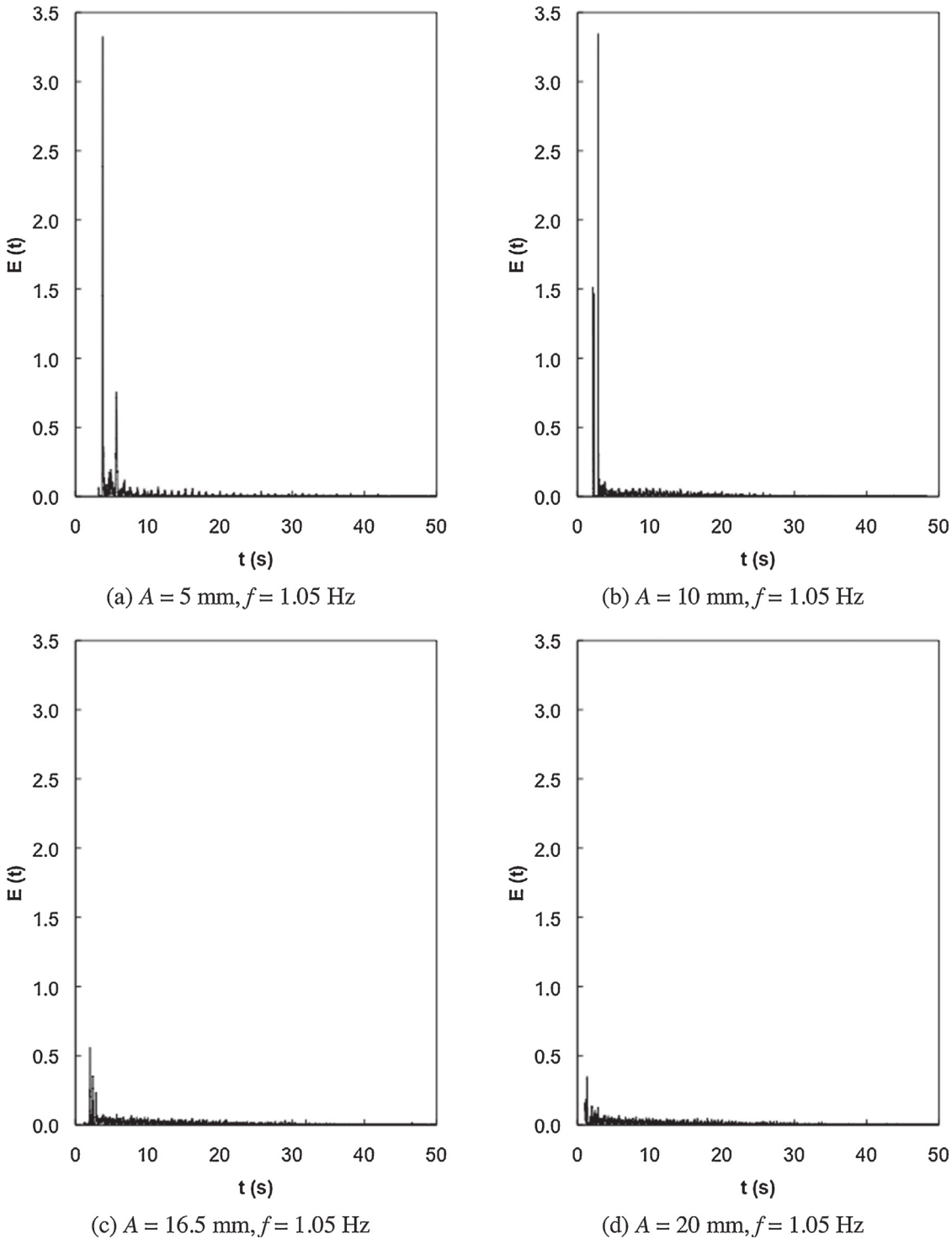

(a) $A = 5$ mm, $f = 1.05$ Hz

(b) $A = 10$ mm, $f = 1.05$ Hz

(c) $A = 16.5$ mm, $f = 1.05$ Hz

(d) $A = 20$ mm, $f = 1.05$ Hz

Fig. 7. Residence time distribution $E(t)$ obtained with the single orifice baffles for different oscillation conditions.

with the single orifice baffles for different oscillatory amplitudes and frequencies are given in Fig. 7.

It can be seen that the maximum value of $E(t)$ decreases with increasing oscillation amplitude and increasing frequency. Among the different operating conditions tested, the highest peaks are obtained for small oscillation amplitudes $A = 5$ mm and 10 mm at $f = 0.635$ Hz (Fig. 7(a,b)). However these peaks are appearing much earlier than the theoretical space-time value, thereby suggesting short-circuiting. For most of the other oscillation conditions the peak is very low or even inexistent, indicating that there is a large spread in the residence time distribution, thereby showing that plug flow is not achieved.

The Péclet numbers and the normalised mean residence times at different oscillatory Reynolds numbers for a fixed net flow rate and reactor length are presented in Fig. 8. It can be seen that in the studied range, the Péclet numbers—and therefore the axial

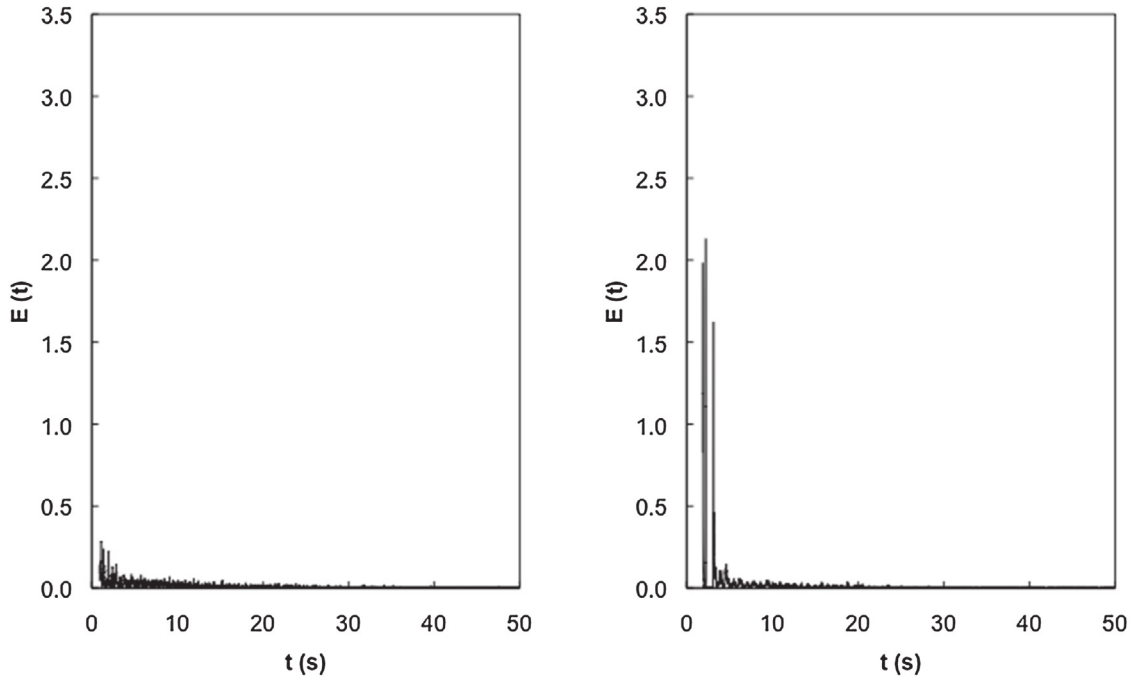

(e) $A = 25$ mm, $f = 1.05$ Hz (f) $A = 16.5$ mm, $f = 0.635$ Hz

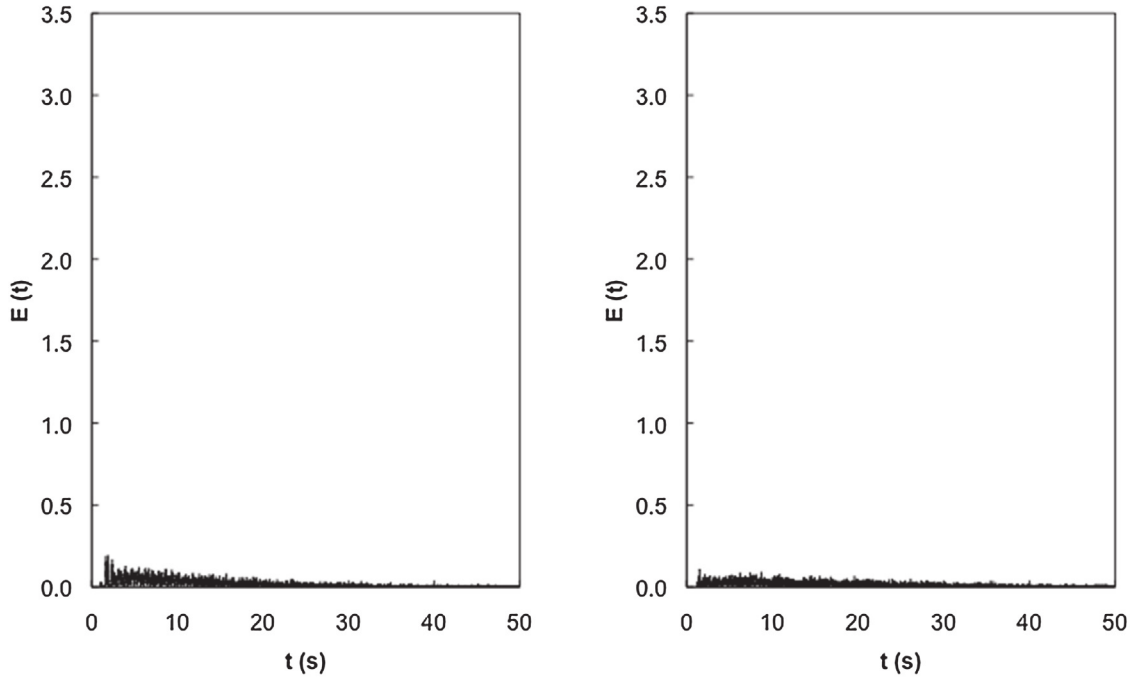

(g) $A = 16.5$ mm, $f = 1.273$ Hz (h) $A = 16.5$ mm, $f = 1.606$ Hz

Fig. 7. (Continued)

dispersion coefficients—vary very little with the oscillatory Reynolds number and hence with oscillation amplitude. For a fixed frequency of 1.05 Hz, the single orifice baffle clearly shows the lowest values of the Péclet number, which are close to one, whilst the central disc in the disc-and-donut configuration clearly limits some axial dispersion, by slightly increasing the Péclet number. At $Re_o = 42$, it is observed that significantly higher Péclet numbers are obtained for the single and alternating helical baffles. When higher oscillating frequencies (e.g. 1.273 Hz and 1.606 Hz) are used with the single orifice and the disc-and-donut baffles, however, the Péclet numbers are greater (and therefore the axial dispersion coefficients are lower) that those obtained at the same oscillatory Reynolds number with $f = 1.05$ Hz. This is surprising considering the shape of the RTD curves for single orifice baffle at these frequencies (Fig. 7(g) and (h)) that show significant distribution, meaning the flow is very different from plug-flow where the tracer

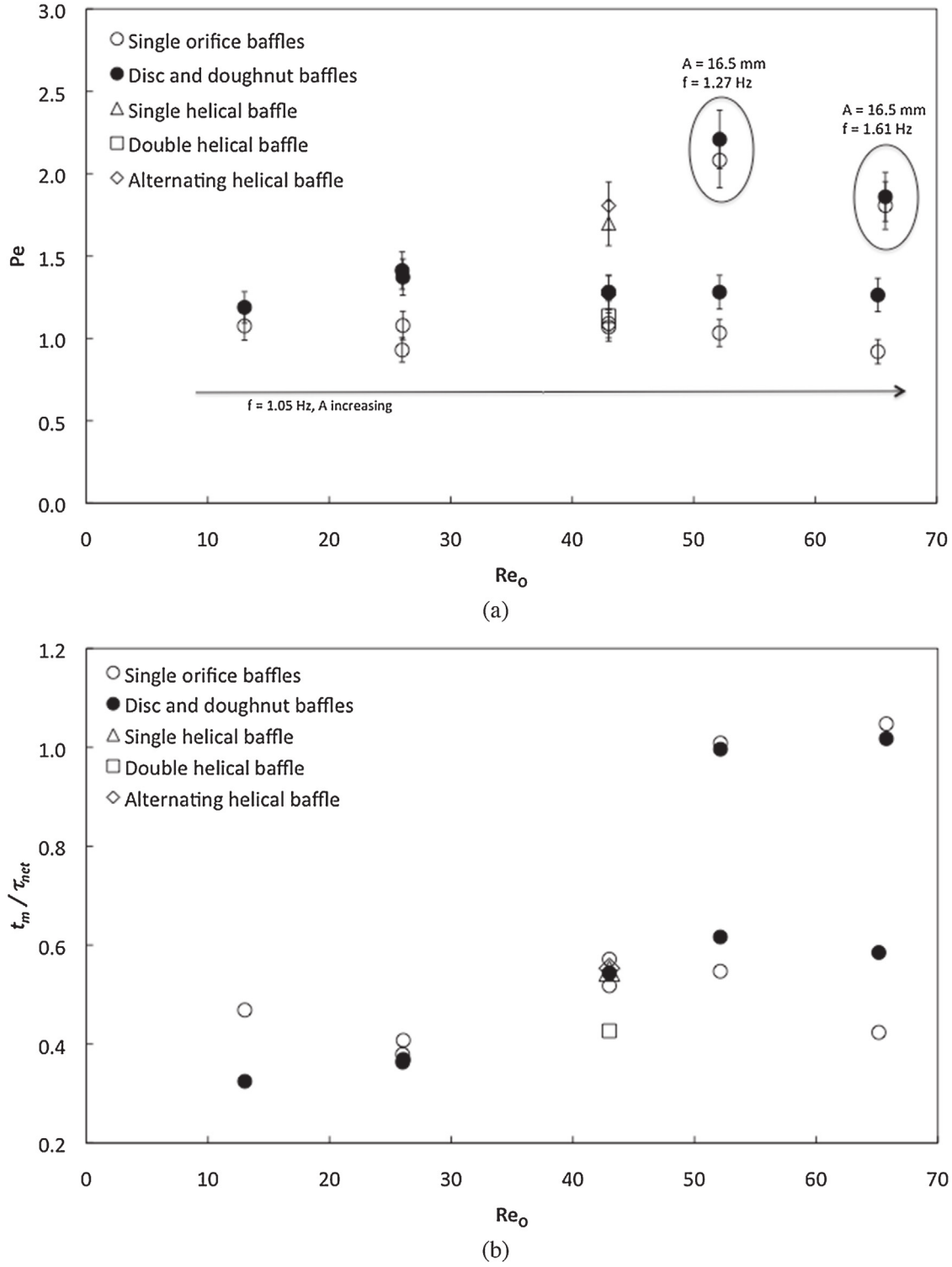

Fig. 8. Effect of Reynolds number on the (a) Péclet number and (b) normalised mean residence time for the different baffle geometries.

would exit at a single instant in time. The associated Péclet numbers are also very low – between 1.1 and 2.2. Indeed, the axial dispersion model for plug flow reactors is valid for Péclet numbers > 10 [18] and this suggests that the model may not be appropriate for high frequencies. Fig. 8(b) shows that the mean residence times are approximately half the theoretical residence time (or space time), which implies the presence of stagnant backwaters and reduced effective reactor volume [18]. Indeed, this can be explained with the velocity fields shown Figs. 4–8 in Part I of this paper that clearly show either closed recirculation loops or zones of low velocity close to the vessel wall, contrasted with significantly fast-flowing fluid in the centre of the tube.

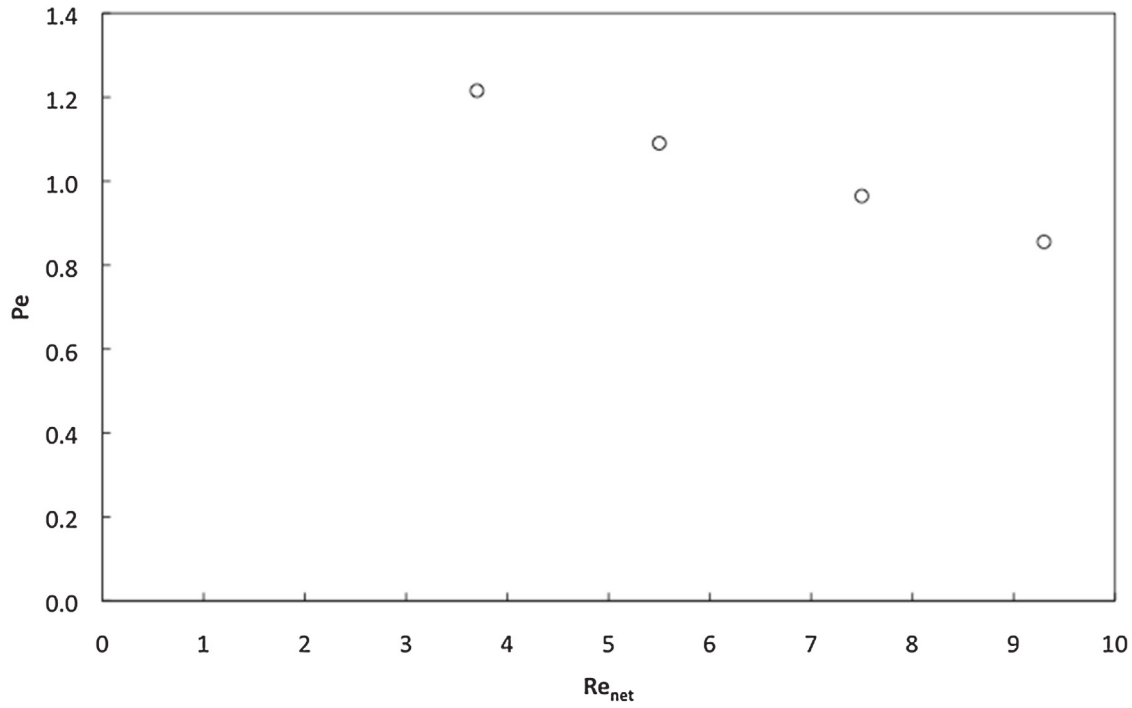

Fig. 9. The Péclet number as a function of the net Reynolds number for fixed oscillation conditions $A = 16.5$ mm and $f = 1.05$ Hz and reactor length L in the single orifice baffled reactor.

Fig. 9 shows the effect of the net Reynolds number (calculated for fixed oscillation conditions ($A = 16.5$ mm and $f = 1.05$ Hz) and reactor length L) on the Péclet number in the single orifice baffled reactor. Although the values are low, the Péclet number clearly decreases with increasing Re_O and therefore flow rate. Indeed, the axial dispersion coefficient increases significantly with the flow rate in this range of Re_O. However with a further increase in flow rate, one would expect a decrease in the dispersion coefficient and consequently an increase in the Péclet number as the flow regime becomes turbulent.

Fig. 10 presents the effect of reactor length on axial dispersion and mean residence time for constant Re_O and Re_{net} in the single orifice reactor. It can be seen that at fixed operating conditions the axial diffusion coefficient remains more or less constant along the reactor with a value that is approximately six orders of magnitude greater than the molecular diffusion coefficient for liquids. This means that for set operating conditions, there is a linear relationship between Péclet number and the reactor length and therefore plug-flow behavior can be achieved by increasing the length of the reactor. For example, in the single orifice baffled reactor with the operating conditions given in Fig. 10 a Péclet number equal to 40, which allows for reasonable plug flow conditions, can be obtained with a reactor length of approximately 6 m. Indeed, the tendency to move toward plug-flow behavior is also shown by comparison of the mean residence time, t_m, with the net space time, τ_{net}, for increasing reactor length as shown in Fig. 10(b). The results show that the mean residence time firstly deviates from τ_{net} with increasing reactor length before converging to the theoretical value. For short reactor lengths the difference between t_m and τ_{net} is due to the high velocity gradients created between the centre of the tube and behind the orifice baffles close to the tube wall. As the tube is made longer, the different fluid elements have the time to sample the variations in velocity and eventually all fluid elements have experienced the same flow on average, thereby leading to $t_m = \tau_{net}$.

5.3. Shear strain rate history

Due to the different baffle geometries and varying velocity gradients, fluid elements can experience significantly different shear strain rates during their time in the reactor. To investigate the differences in strain rates, the time-averaged strain rate, the mean strain rate and the maximum strain rate experienced by the tracer particles have been calculated. Fig. 11 shows the strain rate experienced by the fluid depending on the initial radial position of the fluid element with the alternating helical baffles. It can be seen in Fig. 11(a) that globally over time the different fluid elements experience more or less the same strain rate, which is approximately $40 \pm 5\ s^{-1}$. Fig. 11(b) shows that there is greater spread in the maximum strain rates, however the majority of the fluid experiences maximum strain rates between $150\ s^{-1}$ and $250\ s^{-1}$, which are relatively high values. This means that in this geometry, the ensemble of fluid experiences the same shear rates and that there are no major hydrodynamic passages where fluid experiences globally excessive or weak deformation. This type of analysis may be particularly useful when assessing the capacity of particular baffle geometries to induce or avoid high strain rates and the homogeneity for shear sensitive applications, such as droplet break-up or cell culture.

Fig. 12 shows the influence of the oscillation conditions, via Re_O, and the baffle design on the global mean and the average maximum strain rates. The error bars indicate the standard deviation of the strain rate experienced by the ensemble of particles at each operating condition. It can be seen that the maximum shear strain rate is approximately six times the average value and that the shear strain rate values increase linearly with

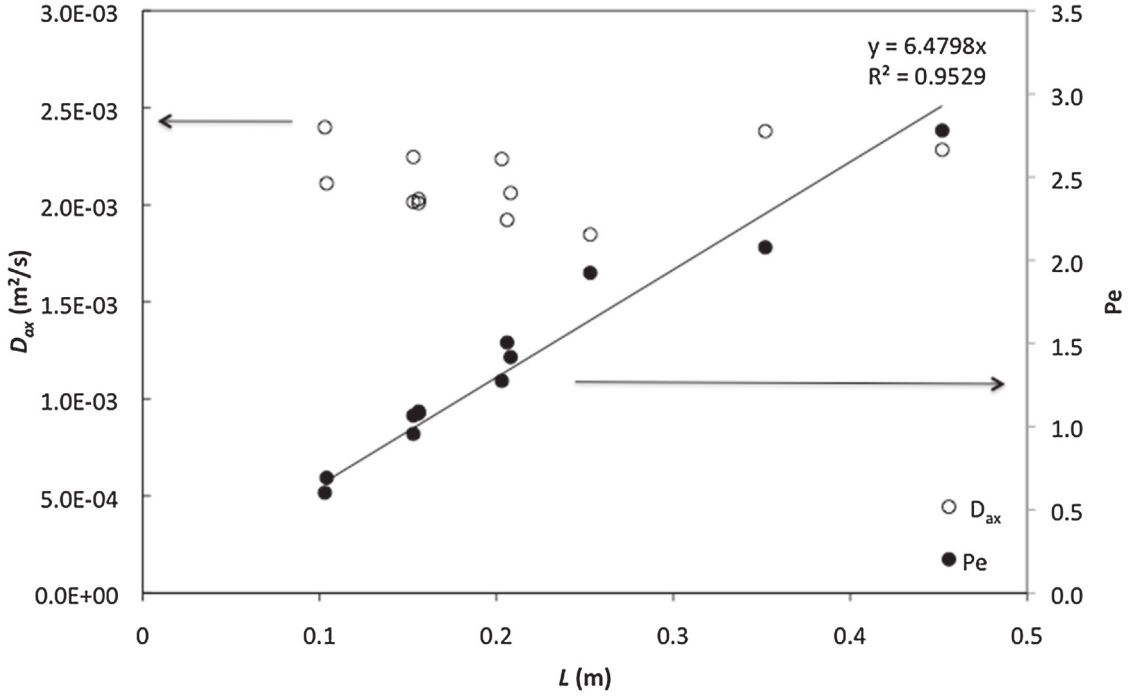

(a)

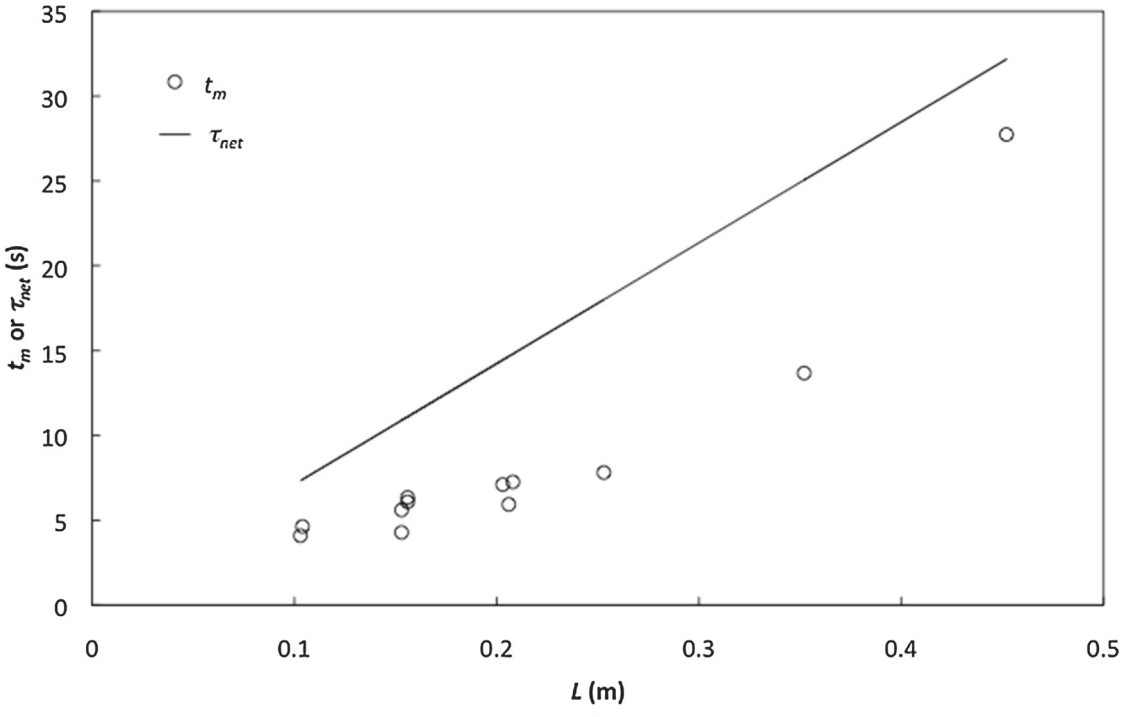

(b)

Fig. 10. Effect of reactor length on (a) the axial diffusion coefficient and (b) the mean residence time for the single orifice baffle geometry with $A = 16.5$ mm and $f = 1.05$ Hz ($Re_O = 43$) and $Re_{net} = 5.5$.

the product *A.f*. This means that high oscillations conditions may be preferred for droplet breakup or solid de-agglomeration applications; however it is important to remember that axial stretching also increases with increasing oscillation conditions so a best compromise may need to be found. An indication of the effect of the different geometries can also be seen at $Re_o = 42$.The disc-and-donut baffles are shown to generate the highest shear strain rates in the reactor, whilst the values for the other designs are lower and vary only slightly. It is interesting to note that the standard deviation is lower for the helical baffle designs, which means there are smaller differences of strain rate experienced by the particles for these geometries. It has also been found that for fixed oscillation conditions and varying flow rate, i.e. Re_{net}, the mean shear strain rate is almost constant and the maximum strain

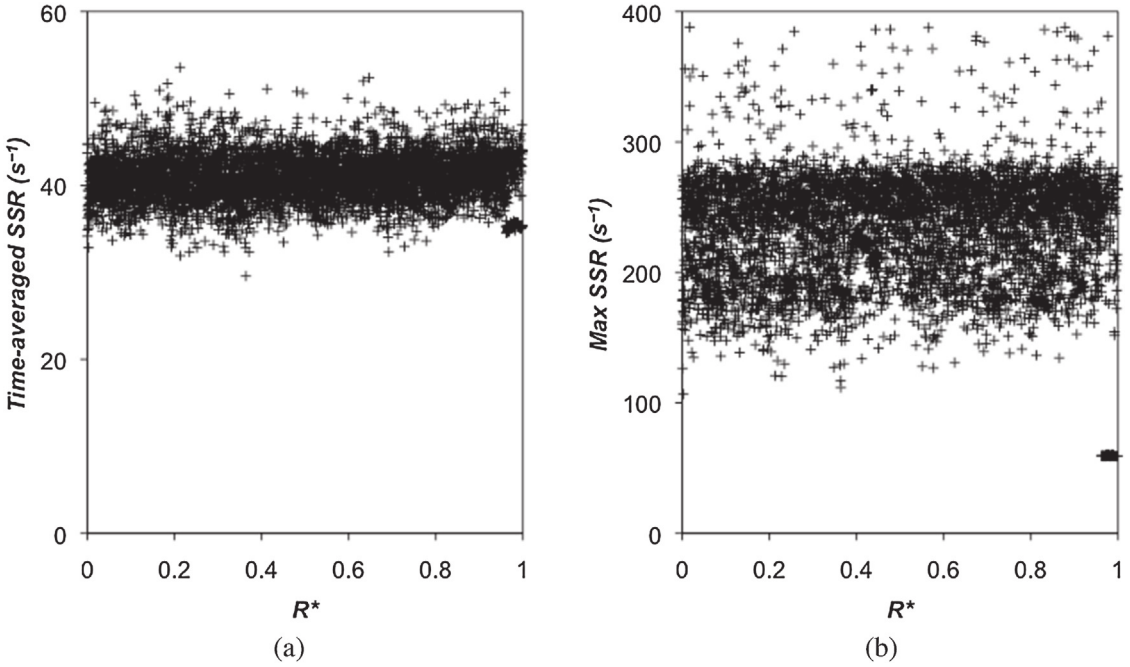

Fig. 11. (a) time-averaged strain rate and (b) maximum strain rate experienced by fluid elements as a function of their initial normalised radial position for the alternating helical baffle geometry with an oscillation amplitude of 16.5 mm and a frequency of 1.05 Hz.

rate increases only very slightly with increasing flow rate. Indeed, shear strain in the reactor is controlled principally by the oscillating conditions.

6. Conclusions

In this work three analysis methods for characterising the flow generated in oscillatory baffled reactors have been developed. These methods analyse axial and radial stretching (and mixing) capacity, shear strain rate history and residence time distribution using data obtained using CFD. Axial and radial stretching is useful to evaluate spatial mixing and the presence of chaotic flow, if required; shear strain rate is useful for applications that are shear-dependent, such as droplet break up, de-agglomeration, applications involving biological cultures; residence time distribution is useful when chemical reactions are being performed. In a general manner, these methods have then been used in this paper to compare the performance of the OBR equipped with novel baffle designs and operating under different flow conditions.

It has been shown that the oscillating conditions, i.e. amplitude and frequency, have a strong effect on certain measures, whereas the flow rate has very little influence. Axial stretching and dispersion, as well shear strain rate increase when the product $A.f$ increases. However, radial stretching and mixing varies very little with this parameter. The Péclet number also varies very little with $A.f$ (when f is constant) but is affected by higher oscillation frequencies.

Comparison of the different baffle geometries with the different performance measures at a single value of Re_o demonstrates the capacity of the measures to differentiate the capabilities of the different designs. At this operating point it is observed that the novel helical type baffles, in particular the single and alternating helical blades, provide slightly less axial stretching and Péclet numbers that are approximately 80% greater than those generated by the single orifice and disc-and-donut baffles. The double helical baffle also enables radial stretching and mixing by 80% compared with the other geometries. Interestingly, the central disc of the disc-and donut-design does not improve radial mixing or decrease axial dispersion significantly compared with the single orifice baffle. The sharp edges (perpendicular to the flow) of the disc-and-donut design do however enable shear strain rates that are around 30% greater than those achieved with the other geometries. Although no firm conclusions can be made at this stage regarding the general performance of the helical designs for a wider range of operating conditions, the characterisation methods provide indications of the characteristics that can be improved with each geometry.

Considering the results on the pressure drop presented in Part I, it appears that the disc-and-donut design induces excessive pressure loss compared with the other geometries without providing a significant gain in performance in terms of radial and axial stretching and residence time distribution. The helical blade designs however provide improved performance in terms of radial mixing and residence time distribution compared with the traditional single orifice baffles for only a small increase in operating costs. Indeed the disc-and-donut baffles appear to be particularly suited to multiphase flow applications where interface generation is required by high shear strain rate. In order to conclude whether the additional operating cost of the disc-and-donut designs for generating dispersions is worthwhile compared with the helical blade baffles, further experimental studies on droplet generation and size would be required.

The ensemble of these results clearly suggest that the baffle geometry of the OBR should be chosen in consideration of the process objectives for best operating performance and that the measurement parameter(s) used to characterise reactor performance should also be chosen depending on the process objective.

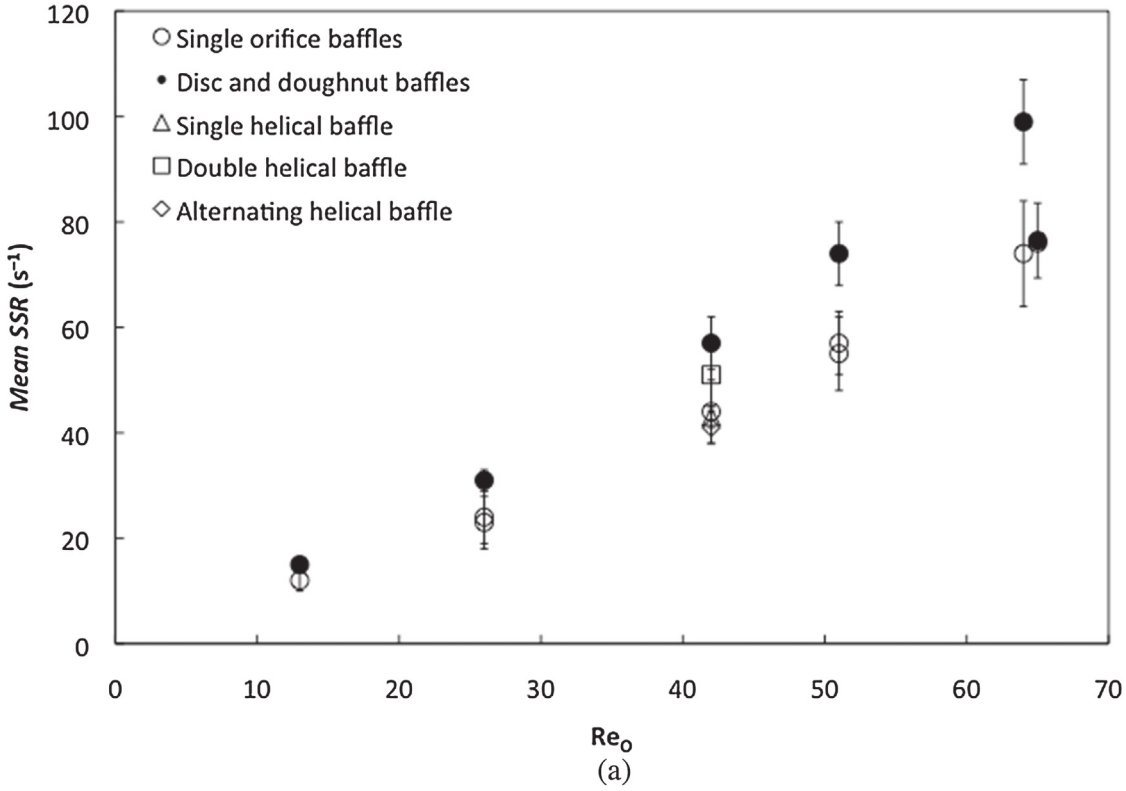

Fig. 12. The effect of baffle geometry on the (a) mean and (b) maximum strain rates experienced in the reactor as a function of the oscillating conditions.

Acknowledgements

This work was part of the AGRIBTP project on bio-products for building and public works funded by the European Union, région Midi-Pyrénées and the French Government. D.F.F. gratefully acknowledges funding from INP Toulouse.

References

[1] A. Mazubert, D.F. Fletcher, M. Poux, J. Aubin, Hydrodynamics and mixing in continuous oscillatory flow reactors—Part I: effect of baffle geometry, Chem. Eng. Proc. PI (2015) Submitted.
[2] X. Ni, H. Jian, A.W. Fitch, Computational fluid dynamic modelling of flow patterns in an oscillatory baffled column, Chem. Eng. Sci. 57 (2002) 2849–2862.
[3] X. Ni, H. Jian, A.W. Fitch, Evaluation of turbulent integral length scale in an oscillatory baffled column using large eddy simulation and digital particle image velocimetry, Trans. IChemE 81 (A) (2003) 842–853.
[4] M. Zheng, J. Li, M.R. Mackley, J. Tao, The development of asymmetry for oscillatory flow within a tube containing sharp edge periodic baffles, Phys. Fluids 114101 (2007).
[5] A.A. Hamzah, N. Hasan, M.S. Takriff, S.K. Kamarudin, J. Abdullah, I.M. Tan, W.K. Sern, Effect of oscillation amplitude on velocity distributions in an oscillatory baffled column (OBC), Chem. Eng. Res. Des. 90 (2012) 1038–1044.
[6] X. Ni, J.A. Cosgrove, A.D. Arnott, C.A. Greated, R.H. Cumming, On the measurement of strain rate in an oscillatory baffled column using particle image velocimetry, Chem. Eng. Sci. 55 (2000) 3195–3208.
[7] P. Stonestreet, P.M.J. Van der Veeken, The effects of oscillatory flow and bulk flow components on residence time distribution in baffled tube reactors, Trans. IChemE 77 (A) (1999) 671–684.
[8] M. Palma, R. Giudici, Analysis of axial dispersion in an oscillatory flow continuous reactor, Chem. Eng. J. 94 (2003) 189–198.
[9] K.B. Smith, M.R. Mackley, An experimental investigation into the scale-up of oscillatory flow mixing in baffled tubes, Chem. Eng. Res. Des. 84 (2006) 1001–1011.
[10] A.N. Phan, A.P. Harvey, Development and evaluation of novel designs of continuous mesoscale oscillatory baffled reactors, Chem. Eng. J. 159 (2010) 212–219.
[11] A.N. Phan, A.P. Harvey, Effect of geometrical parameters on fluid mixing in novel mesoscale oscillatory helical baffled designs, Chem. Eng. J. 169 (2011) 339–347.
[12] A.N. Phan, A.P. Harvey, Characterisation of mesoscale oscillatory helical baffled reactor – Experimental approach, Chem. Eng. J. 180 (2012) 229–236.
[13] A.N. Phan, A.P. Harvey, J. Lavender, Characterisation of fluid mixing in novel designs of mesoscale oscillatory baffled reactors operating at low flow rates (0.3–0.6 ml/min), Chem. Eng. Proc. 50 (2011) 254–263.
[14] X. Nogueira, B.J. Taylor, H. Gomez, I. Colominas, M.R. Mackley, Experimental and computational modeling of oscillatory flow within a baffled tube containing periodic-tri-orifice baffle geometries, Comp. Chem. Eng. 49 (2013) 1–17.
[15] M. Manninen, E. Gorshkova, K. Immonen, X.W. Ni, Evaluation of axial dispersion and mixing performance in oscillatory baffled reactors using CFD, J. Chem. Tech. Biotech. 88 (2013) 553–562.
[16] H.S. Fogler, Elements of Chemical Reaction Engineering, 2nd ed., PTR Prentice Hall, Englewood Cliffs NJ, 1992.
[17] J. Aubin, L. Prat, C. Xuereb, C. Gourdon, Effect of microchannel aspect ratio on residence time distributions and the axial dispersion coefficient, Chem. Eng. Proc. PI 48 (1) (2009) 554–559.
[18] O. Levenspiel, Chemical Reaction Engineering, Wiley, NY, 1999.